Phospholipase D3 regulates TFEB/TFE3 metabolism to maintain lysosomal homeostasis

Yongchao Wang [1*], Paige Rieschick [1], Wilber Romero-Fernandez [1], Nathan Appelbaum [1], Cristian Carvajal-Tapia[1], Alena Shostak [1] and Matthew Schrag [1,2*]

Author affiliations:

[1] Department of Neurology, Vanderbilt University Medical Center, Nashville, TN, USA

[2]Vanderbilt Brain Institute, Vanderbilt University, Nashville TN, USA

[*]Corresponding author: Yongchao Wang and Matthew Schrag

Vanderbilt University School of Medicine

Medical Research Building III

465 21st Avenue S, Suite 61

Nashville, TN 37232

Yongchao.wang@vumc.org and matthew.schrag@vanderbilt.edu

Keywords: Alzheimer's disease (AD); β-amyloid; Phospholipase D3 (PLD3), Transcription factor EB (TFEB); transcription factor binding to IGHM enhancer 3 (TFE3), Lysosomal biogenesis.

Abstract

A coding variant in Phospholipase D3 (*PLD3*) increases the risk of Alzheimer's disease (AD). PLD3 is a lysosomal protein, and endosomal and lysosomal abnormalities are linked to AD; however, the role of PLD3 in lysosomal homeostasis and its implications in AD remain poorly understood. To address this knowledge gap, we conducted comprehensive studies integrating transcriptomics, proteomics, and cell biology approaches. We observed significant enlargement of lysosomes in neurons lacking PLD3, accompanied by increased endocytosis and autophagy, but a decline in lysosomal proteolytic activity. Lysosomes of PLD3-deficient cells underwent proteome remodeling, manifested by an enrichment of proteins involved in lysosomal biogenesis, endocytosis and calcium signaling. Mechanistically, we discovered that PLD3 mediates TFEB/TFE3 degradation through the proteasome, and as a result, PLD3 deficiency leads to increased TFEB/TFE3 levels, nuclear translocation, and transcriptional activities. Notably, variants in PLD3, e.g., V232M or K486R, do not alter its impact on TFEB/TFE3 metabolism. Transcriptomic profiling further confirmed the enrichment of transcripts involved in lysosomal biogenesis, endocytosis, autophagy, mTOR signaling and AD in response to PLD3 loss. Additionally, PLD3 ablation has synergistic effects with β-amyloid in causing lysosomal abnormalities and modifying TFEB/TFE3 signaling. In conclusion, our findings demonstrate that PLD3 is involved in regulating lysosomal biogenesis via TFEB/TFE3 signaling, and lysosomal abnormalities resulting from PLD3 deficiency are potentially a risk factor for AD.

Introduction

Lysosomes are involved in the removal or recycling of proteins, lipids, or organelles through processes like endocytosis, phagocytosis, and autophagy[1,2]. This cellular clearance system is particularly important for neurons due to their high metabolic activity and long lifespan[3]. Irregularities in this clearance system manifest in a variety of genetic and age-related neurodegenerative diseases[4-6]. In patients with sporadic Alzheimer's disease, abnormalities in endosomes and lysosomes, including enlarged neuronal endolysosomal size, were observed prior to the appearance of typical pathologies such as amyloid plaques and tau tangles[7]. Moreover, studies using preclinical animal models demonstrated that endosomal and lysosomal activities were only minimally influenced by normal aging[7]. These findings indicate that endosomal and lysosomal abnormalities are potentially an upstream driver of AD. Indeed, a new model of

Alzheimer's disease (AD) proposes that major AD pathologies may arise, in whole or in part, from defective proteostasis caused by endolysosomal failure[8]. Given the numerous clinical trials targeting β-amyloid pathology that have either failed or produced minimal efficacy in Alzheimer's disease patients[9], the endolysosomal system may emerge as a prime target for the next generation of drug development in neurodegenerative disorders.

As a defining feature of AD, β-amyloid (Aβ) pathology has been the focus of AD research for decades. The endosomal and lysosomal system plays a crucial role in the processing of amyloid precursor protein (APP) and the formation of Aβ peptides. Specifically, APP traffics from the cell surface via endosomes, along with β-secretase and other molecular machinery required for Aβ production[10]. The acidic environment within late endosomes and lysosomes facilitates Aβ aggregation, potentially leading to the formation of amyloid fibrils and plaques[11,12]. Additionally, lysosomal nuclease activities influence nucleotide signaling, which in turn affects APP processing through downstream cGAS-STING activation[13]. The endosomal and lysosomal system is also indirectly involved in Aβ production. For example, cholesterol transport and metabolism, facilitated by endosomes and lysosomes, affect the function of various receptors and transporters involved in Aβ clearance[14-16]. The phagocytic receptor, Trem2, depends on endosomal recycling to traffic to the microglial cell surface, where it plays a role in the removal of Aβ plaques[17]. Hence, abnormalities in the endosomal and lysosomal systems may contribute to Aβ pathology.

PLD3 is a homolog of the phospholipase D family[18], localized to lysosomes through an unconventional pathway[19]. Its role in lipid metabolism has recently been confirmed to be associated with the formation of bis(monoacylglycero)phosphate (S,S-BMP)[20], which is essential for ganglioside metabolism. PLD3 is predominantly expressed in neurons of cortical and hippocampal regions[21,22], while its counterpart, PLD4, is mainly expressed in peripheral immune cells. These distinct expression patterns correlate with their roles in different biological and pathological conditions. PLD3 is more associated with neural function and related disorders, whereas PLD4 is primarily linked to immune response and autoimmune conditions[23-25]. At least one coding variant in *PLD3* is convincingly linked to increased risk of AD[26]. We discovered that

PLD3 is significantly enriched in dystrophic neurites surrounding β-amyloid plaques, and its expression correlates with cognitive function in both human and animal studies[24]. More recently, PLD3 was functionally linked to the formation and growth of dystrophic neurites, contributing to neural network defects in AD[23]. The lysosomes in neurons of *PLD3* knockout mice exhibited significant enlargement[27]. Our group recently showed that PLD3 controls cathepsin B activity and trafficking, correlating its deposition alongside vasculature with the pathological phenotypes in AD. Therefore, PLD3 is clearly involved in lysosomal function in neurons, but its role in lysosomal homeostasis and the potential implications for Alzheimer's disease (AD) remain incompletely understood.

TFEB and TFE3 govern the expression of a network of genes linked to lysosomal biogenesis and autophagy. Their transcriptional activities are controlled by a two-pronged cellular mechanism. Specifically, TFEB and TFE3 can be phosphorylated and sequestered by mTOR complex 1(mTORC1) and 14-3-3 protein respectively, trapping them in the cytoplasm[28]. Conversely, dephosphorylation by calcineurin or extracellular signal-regulated kinase 2 (ERK2) promotes their nuclear translocation, enabling them to exert transcriptional function[29]. Various cellular stresses, such as nutrient deprivation, oxidative stress, and accumulation of misfolded proteins, can influence TFEB and TFE3 signaling, promoting the expression of genes, including those involved in lysosomal function and autophagy, that facilitate the adaptation to these cellular stresses[30]. In addition to the regulation via post-translational modification, TFEB and TFE3 signaling can also be controlled through protein turnover by the ubiquitin-proteasome degradation system[31]. For example, phosphorylation of TFEB by the IκB kinase (IKK) complex can trigger its ubiquitination mediated by β-transducin repeat-containing protein 2 ((β-TrCP2)) for degradation[32]. In the context of AD, it has been reported that genetic disruption of TFEB results in defective microglia activation and increased tau pathology[33]. Nevertheless, the connection between PLD3 and TFEB/TFE3 signaling, and its association with AD remain poorly understood.

In this study, we generated *PLD3* knockout neuroblastoma cells and examined the impact of *PLD3* deletion on neuronal lysosomal homeostasis and function using biochemical, immunohistochemical, and transmission electron miscopy (TEM) approaches. We also

conducted proteomic studies to comprehensively assess lysosomal alterations at proteome level in the context of PLD3 knockout. To interrogate the underlying mechanisms, we explored the involvement of PLD3 in TFEB/TFE3 signaling. Finally, we translated our findings from in vitro cell models to human AD samples, underscoring their clinical relevance and significance.

Results

Loss of PLD3 alters lysosomal homeostasis and functions.

Because PLD3 is predominantly expressed in neurons[18], we employed a neuroblastoma cell line, SH-SY5Y, as the cellular model to investigate the role of PLD3 on lysosomal homeostasis and function. We generated *PLD3* knockout (KO) cell lines, clone 3 and clone 4, through CRISPR/Cas9 editing and validated *PLD3* deletion in these clones by western blot of PLD3 (Fig. 1A). Lysosomal attributes such as size, density and confluency in these cells were characterized by transmission electron microscopy (TEM). The size of individual lysosomes in KO cells exhibited significant enlargement compared to wild-type (WT) cells (Fig. 1B). In agreement with this, lysosomal density and confluency expressed by the number of lysosomes per unit area and the percentage of occupied area, respectively, were also markedly increased following *PLD3* KO (Fig. 1B). Lysosomal acidity levels were evaluated using the ratio of two fluorophores, Oregon Green (pH-sensitive) and Alexa 594 (pH-insensitive), which were trafficked to lysosomes by conjugation to dextran. Dextran localization to lysosomes was confirmed by colocalization and correlation analysis between the dextran signal and LAMP1-RFP (Suppl Fig. 1). We did not observe a significant change in pH levels of lysosomes in *PLD3* KO cells (Fig. 1C). Aligned with the findings from TEM, lysosome size and confluency were also increased, although a significant increase in lysosome density was not detected in lysosomal labeling with dextran (Fig. 1C). Corresponding with the overall increase in lysosome volumes, lysosome-related cellular processes, such as endocytosis and autophagy, were also enhanced in KO cells, as evidenced by increased dextran engulfment and LC3B-II levels (Fig. 1C and 1E). However, a broad assessment of lysosomal protease activities, measured by DQ assay, revealed a functional decline in KO cells compared to WT cells (Fig. 1D). Collectively, these results suggest that PLD3 loss leads to an increase in lysosomal volume and potentially a modification in global lysosome function.

Loss of PLD3 induces remodeling of the lysosomal proteome.

To comprehensively characterize the lysosomes, we isolated lysosomes from these cells using dextran-coated superparamagnetic iron oxide (SPIO) nanoparticles and magnetic chromatography, followed by label-free proteomic studies on the lysates of lysosomal fractions. We first examined the enrichment of lysosomal proteins in subcellular fractions via western blotting. Lysosomal signature proteins, including cathepsin D (CTSD), cathepsin B (CTSB), and LAMP2, were highly enriched in the lysosomal fraction, while cytosolic-specific-proteins like β-tubulin were absent (Fig. 2A). Additionally, compared to the WT cells, lysosomes from *PLD3* KO cells exhibited a significantly higher expression of these lysosome-specific proteins (Fig. 2A). Proteomic analysis of these lysosomal lysates identified 3,075 proteins (Suppl File 1). Among them, 81 were significantly upregulated in *PLD3* KO cells compared to WT cells, while 72 were significantly downregulated (Fig. 2B). Gene set enrichment analysis revealed that signaling pathways related to lysosomes, including lysosomal biogenesis, endocytosis and calcium signaling, were significantly enriched in *PLD3* KO cells compared to WT cells (Fig. 2C-E, Suppl Fig. 2B-D). *PLD3* KO cells were also enriched in vesicle trafficking proteins, such as SNARE (Soluble NSF Attachment Protein Receptor) interaction proteins, which are involved in the fusion of vesicles with early endosomes, late endosomes, and lysosomes (Fig. 2C). Notably, we also observed that sphingolipid metabolism signaling, and proteins relevant to AD were differentially enriched between WT and KO cells, indicating a role of PLD3 in phospholipid metabolism and AD pathogenesis (Fig. 2C). Taken together, our proteomic analysis results demonstrated that PLD3 ablation induces lysosomal proteome remodeling, featuring an enrichment of lysosome-related signaling, membrane trafficking, phospholipid metabolism and AD-related proteins.

PLD3 regulates TFEB/TFE3 degradation through the proteasome rather than lysosomes.

Mechanistically, because we observed an increase in lysosome volume and elevated levels of proteins related to lysosome biogenesis, we hypothesized that PLD3 might play a role in lysosomal biogenesis. TFEB/TFE3 are master regulators of lysosomal biogenesis and autophagy[34], so we prioritized our investigation to explore the impact of PLD3 on TFEB/TFE3 signaling. We first assessed mRNA levels of TFEB and TFE3 and found no significant difference between WT and KO cells, suggesting that any potential regulation of TFEB and

TFE3 by PLD3 does not occur at transcriptional level (Suppl Fig. 3A). In contrast, TFEB and TFE3 protein levels were markedly elevated in *PLD3* KO cells compared to WT cells under various conditions, including no stimulation (NS), dextran treatments to induce endocytosis, nutrient starvation (HBSS) and Torin 1 treatment to induce autophagy (Fig. 3A and Suppl Fig. 3B). Exogenous TFEB, expressed as GFP N-terminal tagged TFEB, also showed increased expression in *PLD3* KO cells versus WT cells (Fig. 3B). Additionally, the expression trends in TFEB and TFE3 observed upon *PLD3* knockdown (KD) by siRNAs were similar to those seen in *PLD3* KO cells compared to WT cells (Suppl Fig. 3C). Consistent with these results, the overexpression of PLD3 in HeLa cells led to a significant reduction in TFEB and TFE3 levels (Fig. 3C). Interestingly, variants in PLD3, e.g., V232M or K486R, did not alter its effects on TFEB metabolism (Fig. 3C). In summary, these data suggest that PLD3 is involved in TFEB/TFE3 protein metabolism, and *PLD3* KO leads to their accumulation.

Having identified PLD3 as a regulator of TFEB/TFE3 metabolism in neurons, we next sought to elucidate the mechanisms by which it controls TFEB/TFE3 degradation. We investigated the potential involvement of the proteasome and/or lysosomes in this process. Treatment with MG132, a proteasome inhibitor, caused significant accumulation of TFE3 and, more importantly, resulted in comparable levels of TFE3 between WT and KO cells at all three time points (Fig. 4A-C). This suggests that PLD3 facilitates TFE3 degradation via the proteasome. In contrast, TFEB levels declined over time following MG132 treatment, indicating that the proteasome was indirectly involved in PLD3-mediated TFEB metabolism (Fig. 4A-C). Treatment with another proteasome inhibitor, Bortezomib, produced similar effects on TFEB/TFE3, further confirming the involvement of proteasome in PLD3-mediated TFEB/TFE3 degradation (Suppl Fig. 4A and 4B). To specifically focus on protein metabolism, we blocked protein translation using cycloheximide (CHX) and assessed TFEB/TFE3 levels following MG132 treatment. MG132 generated similar effects on TFEB/TFE3 with the arrest of protein translation, supporting the conclusion that the proteasome is involved in PLD3-mediated TFEB/TFE3 protein metabolism (Fig. 4D). Interestingly, CHX treatment led to a sharp decline in TFE3 levels but a gradual decrease in PLD3 and TFEB levels, suggesting that TFE3 is a short-lived protein, while TFEB and PLD3 are long-lived proteins (Fig. 4D). Immunoprecipitated (IP) TFE3 showed heightened ubiquitination in WT cells versus KO cells upon MG132 treatment, aligning with the assertion

that PLD3 facilitates the ubiquitination-mediated degradation of TFE3 (Fig. 4E). Concerning the potential involvement of lysosomes in TFEB/TFE3 metabolism, treatments with lysosome alkalinizing agents, chloroquine (CQ) or bafilomycin A1 (BAF), exhibited no significant effects on TFEB/TFE3 levels, which suggests that these proteins are not degraded via lysosomal pathways (Fig. 4F and 4G). Nevertheless, we did observe an accumulation of TFE3 after prolonged exposure to CQ or BAF. This could possibly be due to an induction of lysosomal stress following CQ or BAF exposure, which in turn activated TFE3 signaling, rather than producing a direct impact on TFE3 protein metabolism (Fig. 4F and 4G).

Collectively, this data suggests that PLD3 facilitates TFEB/TFE3 protein metabolism via the proteasome.

Loss of PLD3 enhances nuclear translocation and transcriptional activity of TFEB/TFE3.

After demonstrating that TFEB/TFE3 protein levels were increased in PLD3 KO cells, we evaluated whether this led to altered TFEB/TFE3 signaling, including nuclear translocation and transcriptional activities. We first assessed TFEB/TFE3 levels in the cytoplasmic (CE) and nuclear (NE) compartments using western blotting. Under basal conditions and conditions known to induce autophagy, such as nutrient deprivation (HBSS) or mTOR inhibition (Torin 1), the protein levels of TFEB/TFE3 in the nuclear compartment of KO cells were much higher than those in WT cells (Fig. 5A). However, we did not find a significant difference in terms of the protein ratio of nuclear TFEB/TFE3 to cytosolic TFEB/TFE3 between WT and KO cells (Fig. 5A). Surprisingly, we observed significant nuclear localization of PLD3 in WT cells, which may challenge the claim of its exclusive lysosomal localization (Fig. 5A). Immunocytochemical staining of TFEB confirmed these findings, showing increased TFEB levels and nuclear translocation in KO cells compared to WT cells (Fig. 5B). Exogenous TFEB, expressed as GFP N-terminal tagged TFEB, also exhibited increased nuclear translocation in KO cells versus WT cells, with or without Torin 1 treatment (Suppl Fig. 5A). Corresponding to the increased nuclear translocation of TFEB/TFE3, the transcription of their targeted genes, which contain coordinated lysosomal expression and regulation (CLEAR) motif, were also augmented (Fig. 5C) in KO cells compared to WT cells. Moreover, the mRNA levels of two genes, RRAGD and GPNMB, known to respond to TFEB, were markedly upregulated (Fig. 5D). The transcriptional upregulation of

these genes was also confirmed upon *PLD3* knockdown by *PLD3* siRNAs (Suppl Fig. 5B and 5C). In summary, these results suggest that, consistent with the increased levels of TFEB/TFE3 in KO cells, their transcriptional activity is also elevated.

PLD3 deficiency increases signaling related to lysosomes and Alzheimer's disease.

We then examined the impact of PLD3 deficiency on the cellular transcriptome. Total RNA from WT and KO cells underwent RNA sequencing, followed by differential gene expression (DGE) analysis and gene set enrichment analysis (GSEA). The sequencing data was summarized into 60,662 genes. Of these, 7,673 genes were differentially expressed between WT and KO cells, with 4,015 upregulated and 3,658 downregulated (FDR<0.05; Suppl Fig. 6B and 6C). The upregulated genes were primarily associated with signaling pathways involved in cell-cell interaction, neural development and inflammatory conditions (Suppl Fig. 6D). In alignment with our proteomic analysis, signaling pathways related to lysosomal biogenesis, endocytosis and AD were also upregulated in PLD3 KO cells compared to WT cells, although their significance did not reach the FDR<10% threshold (Suppl Fig. 6D-F). To explore the immediate transcriptomic changes associated with the milder phenotype resulting from PLD3 deficiency, *PLD3* was knocked down in SH-SY5Y cells, followed by RNA sequencing and the aforementioned analyses. We first verified *PLD3* knockdown (KD) through western blot of PLD3 (Suppl Fig. 7A). Compared to control siRNAs (CTL), all three *PLD3* siRNAs achieved 60-90% knockdown of *PLD3* (Suppl Fig. 7A). DGE analysis revealed 2,830 genes that were differentially expressed between *PLD3* KD and CTL cells (Suppl Fig. 7B and 7C). Among them, 2,118 genes were upregulated and 712 genes were downregulated in *PLD3* KD cells compared to CTL cells (FDR<0.05; Suppl Fig. 7B and 7C). We also observed significant enrichment in signaling pathways associated with lysosome and autophagic flux, such as lysosome biogenesis, endocytosis, mTOR signaling, and autophagy signaling, in *PLD3* KD cells relative to CTL cells (Fig. 6A and 6B). Additionally, signaling pathways that were previously reported to be associated with PLD3 or lysosomes, including those involved in inflammatory & immune signaling, protein or energy metabolism, and AD, were also differentially enriched between *PLD3* KD cells and CTL cells (Fig. 6A). The transcripts associated with lysosome biogenesis and AD pathologies were illustrated in Fig. 6C and 6D, showing a significant increase in *PLD3*

KD cells when compared to CTL cells. Overall, these findings demonstrate that, at the transcriptome level, PLD3 is linked to lysosomal biogenesis, autophagic flux and AD signaling.

Loss of PLD3 intensifies amyloid-induced lysosomal abnormality and TFEB signaling.

One of the defining features of AD is the presence of Aβ plaques in the brain,[5,35] and while they are spatially closely related to lysosomal abnormalities in the brain, their effects on lysosomal function are incompletely understood. In this study, using neuroblastoma-derived neurons, we explored the effects of Aβ on lysosomal homeostasis. Neurons exposed to Aβ seeds derived from cerebral amyloid angiopathy (CAA) patients for 5 days exhibited significant enlargement of individual lysosomes and an increase in total lysosome volumes per neuron, even though no significant changes were observed in lysosomal pH and localization (Fig. 7A). Morphological examination and transcriptomic profiling suggested that deficiency in PLD3 had minimal impact on the neuronal differentiation of SH-SY5Y cells (Suppl Fig. 8A and 8B). Next, we examined TFEB/TFE3 signaling in neuroblastoma cells following exposure to synthetic Aβ1-42 at various time intervals. In both WT and KO cells, Aβ exposure started to mediate TFEB/TFE3 nuclear translocation on day 3 though day 7 (Fig. 7B). More importantly, the baseline levels of TFEB/TFE3 as well as their nuclear translocation in response to Aβ exposure were much higher in *PLD3* KO cells compared to those in WT cells (Fig. 7B). The effects of PLD3 on lysosomal homeostasis may have implications for its role in the pathogenesis of AD. Our proteomic data and RNASeq data indicates that PLD3 KO enhances AD-related signaling (Fig. 2C, Fig. 6A and Suppl Fig. 7D). Additionally, TFEB levels in the brains of AD patients were significantly higher compared to non-AD patients, showing a negative correlation with the decrease of PLD3 (Fig. 7C). However, this pattern and trend were not observed for TFE3 (Fig. 7C). Collectively, these results demonstrate that Aβ influences lysosomal homeostasis, and PLD3 deficiency exacerbates Aβ's effects on lysosomal alteration and TFEB signaling, which may have implications for the pathogenesis of AD.

Discussion

Our data support a critical role of PLD3 in regulating lysosomal homeostasis in neurons. Deletion of *PLD3* leads to lysosomal abnormalities, manifested by enlargement in lysosomal size and remodeling of lysosomal proteome. Concomitant with enlarged lysosomes are increased

endocytosis and autophagy but a decreased proteolytic capacity of lysosomes. The molecular underpinnings involve TFEB/TFE3, where the loss of PLD3 leads to reduced degradation of these factors via the proteasome, resulting in increased signaling. Finally, we demonstrate that PLD3 potentially correlates negatively with TFEB/TFE3 in the neurons affected by AD, and PLD3 deficiency exerts synergistic effects with Aβ in causing lysosomal abnormalities and modifying TFEB signaling. Given that a variant in *PLD3* is recognized as an AD risk gene, these findings enhance our understanding of its mechanistic basis and may pave the way for developing targeted treatments for AD.

Loss of function in PLD3 has been demonstrated to lead to an enlargement of lysosomes in animal models of AD[27]. However, the underlying mechanisms and its implications in AD remain elusive. Our studies addressed this gap by demonstrating that PLD3 is involved in the metabolism of TFEB/TFE3 in neurons, and that deficiency in PLD3 results in increased signaling in TFEB/TFE3 pathways. TFEB/TFE3 are master regulators of lysosomal biogenesis and autophagy; their signaling activation promotes lysosome production[30,36,37]. We believe that the enlargement of lysosomes is a risk factor for AD as it may interfere with their axonal trafficking. Previous studies have demonstrated that axonal accumulation of endolysosomal vesicles leads to the formation of dystrophic neurites (also referred to as axonal spheroid), which causes the blockade of neural network function in AD[23]. This is also supported by our results from proteomic analysis of lysosomal proteins and RNA sequencing analysis of the whole transcriptome, which indicate that signaling pathways relevant to AD are enriched in *PLD3* KO cells. Notably, while lysosomes are enlarged due to PLD3 deficiency, their overall proteolytic capacity is compromised, which is aligned with the finding in microglia cells[20]. Thus, we conclude that PLD3 is a crucial regulator of lysosome structure and abundance, and its deficiency potentially modifies lysosomal function.

TFEB and TFE3 are members of the MiT (microphthalmia-associated transcription factor) family, sharing significant similarity in structural domains[38,39]. They play a key role in lysosomal biogenesis, autophagy, and cellular metabolism. Their activities are controlled by mTORC1 and calcineurin, which regulate the phosphorylation and subcellular localization of TFEB /TFE3[28,29]. Unlike conventional lysosomal stressors, such as amino acid deprivation, the deletion of *PLD3*

did not significantly impact mTOR and calcineurin activities. The phosphorylation level of endogenous TFEB at Ser 142 and Ser211 were undetectable in SH-SY5Y cells (Suppl Fig. 3D). However, we observed a marked increase in TFEB and TFE3 protein levels, but not mRNA levels, and corresponding nuclear translocation upon PLD3 ablation, suggesting that PLD3 regulates TFEB/TFE3 metabolism at the protein level. Taken together, these data suggest that the observed increase in lysosomal biogenesis is not due to compensatory effects from lysosomal stress, as indicated by increased phosphorylation and nuclear translocation of TFEB/TFE3 typically seen with conventional lysosomal stressors[30,36]. Instead, it appears to be a consequence of TFEB/TFE3 accumulation due to impaired catabolism resulting from PLD3 deficiency. We further demonstrated that PLD3 mediates the degradation of TFEB and TFE3 via the proteasome rather than through lysosomal degradation. While ubiquitin-mediated degradation of TFEB via proteasome has been reported to be initiated by phosphorylation of TFEB by the IKK complex[32], our study did not show significant changes in IKKα/β, and their phosphorylated levels were undetectable in our cellular models (Suppl Fig. 4C and 4D). These findings indicate that the upstream regulators of TFEB metabolism may vary depending on cellular context and stimuli. Additionally, our data suggest an indirect involvement of the proteasome in TFEB metabolism, as proteasome inhibitors were observed to promote, rather than inhibit, TFEB degradation. We speculate that certain proteins metabolized through the proteasome may target TFEB for degradation. Further studies are warranted to delineate the specific mechanisms by which the proteasome influences TFEB metabolism. Moreover, because PLD3 is primarily localized in lysosomes[19], it will be important to identify the mediators that transmit signals from lysosomes to TFEB and TFE3.

Endosomal and lysosomal irregularities have been observed in various cellular and animal models simulating AD, as well as in the brains of AD patients[7,40-42]. The genetic underpinnings were recently mapped out by genome-wide meta-analysis[43]. Moreover, increasing evidence suggests that endosomal and lysosomal abnormalities are central to various AD pathologies, including β-amyloid and tau pathology, synaptic dysfunction, and microglial dysfunction[8]. This assumption is supported by the crucial roles of endosomal recycling and lysosomal clearance in the processing and removal of aberrant β-amyloid and tau proteins, as well as in the transport of synaptic vesicles and phagocytic receptors[10,44]. Previous studies showed that *PLD3* deletion did

not significantly alter full-length APP and c-terminal APP (C-APP), despite the presence of abnormal lysosomes. This suggests that the lysosomal changes caused by *PLD3* deletion may not be severe enough to impact APP processing[27]. On the other hand, our findings with neuroblastoma-derived neurons demonstrate that prolonged exposure to β-amyloid seeds (isolated from human brain tissue with CAA) leads to lysosomal enlargement. Additionally, the combined effects of PLD3 loss and β-amyloid seeds show a synergistic impact on lysosomal alterations. These phenotypic changes in lysosomes correlate with alterations in TFEB and TFE3 pathways. Overall, these findings strengthen the connection between Aβ pathology and lysosomal dysfunction, and, more importantly, reveal a regulatory role for PLD3 in their interplay.

This study underscores the importance of PLD3 in maintaining lysosomal homeostasis in neurons. The findings are particularly significant given the pivotal role of the endosomal and lysosomal system in causing or mediating other AD pathologies, including Aβ and tau pathologies[8]. Our study provides a mechanistic basis by highlighting the involvement of TFEB/TFE3 signaling. Because PLD3 is a lysosome-resident protein in neurons, future studies could focus on identifying mediators that transmit signals from lysosomes to TFEB/TFE3. Additionally, microglial cells mediate phagocytosis and inflammation induction, which play a significant role in the pathogenesis of AD[45,46]. While PLD3 is primarily expressed in neurons, its expression in microglial cells is induced upon microglial activation[47,48]. Growing evidence has confirmed the involvement of PLD3 in inflammatory conditions[25,49]. Hence, future research efforts could focus on exploring PLD3's function in microglial cells and its association with phagocytosis, inflammation induction and their interplay with Aβ and tau pathologies.

Materials and Methods

Human brain samples

Human brain samples were procured from the Vanderbilt Brain Bank at Vanderbilt University Medical Center in Nashville, Tennessee, USA (IRB# 180287). Consent for brain donation was provided in writing from either the patients themselves or their designated decision-makers. All procedures were approved by Institutional Review Board at Vanderbilt University Medical

Center and conducted in compliance with the ethical guidelines outlined in the World Medical Association's Declaration of Helsinki for research using human samples.

Antibodies and reagents

Primary antibodies used in this study include: rabbit anti-PLD3 (HPA012800, Sigma, 1:1000 for WB), mouse anti-TFEB (91767, Cell Signaling Technology, 1:1000 for WB, 1:100 for IF), rabbit anti-TFE3 (81744, Cell Signaling Technology, 1:1000 for WB), mouse anti-Lamin B1 (66095, Proteintech, 1:1000 for WB), mouse anti-LC3B (83506, Cell Signaling Technology, 1:1000 for WB), mouse anti-LAMP2 (H4B4, DSHB, 1:1000 for WB), mouse anti-GAPDH (ab59164, Abcam, 1:5000 for WB), rabbit anti-β-tubulin (15115, Cell Signaling Technology, 1:5000 for WB), goat anti-LCTSB (AF965, R&D systems, 1:1000 for WB), goat anti-CTSD (AF1014, R&D systems, 1:1000 for WB), mouse anti-ubiquitin (13-1600, Invitrogen, 1:1000 for WB), rabbit anti-IKKβ (8943, Cell Signaling Technology, 1:1000 for WB), normal rabbit IgG (12-370, Cell Signaling Technology), dextran Oregon Green 488 (D7172, ThermoFisher Scientific), Protein G/A agarose supernatant (IP05, Millipore), dextran Alexa Fluor 594 (D22913, ThermoFisher Scientific), dextran Alexa Fluor 647 (D22914, ThermoFisher Scientific), CellLight Lysosome-RFP BacMam 2.0 (C10597, ThermoFisher Scientifc), Torin 1(14379, Cell Signaling Technology), Hoechst 33342 (R37605, ThermoFisher Scientific, 2 drops/ml), neurobasal-A medium, minus phenol red (12349015, ThermoFisher Scientific) and β Amyloid 1-42, aβ, recombinant human (AG968, Sigma). The information for all other reagents is indicated in corresponding sections.

Cell culture, plasmids, and siRNA transfection

SH-SY5Y neuroblastoma cells were from ATCC (CRL-2266) and cultured in DMEM/F12 media supplemented with 10% FBS and 1% penicillin/streptomycin. *PLD3* plasmids were from Sino Biological and the *PLD3* mutant plasmids were generated using site-directed mutagenesis kit as described previously. GFP-N-TFEB (38119, Addgene) and its corresponding control (60360, Addgene) plasmids were from Addgene. *PLD3* siRNAs and their corresponding control siRNAs were purchased from IDT. For plasmid transfection, plasmid DNA was transfected into cells with Lipofectamine 3000 reagent following the manufacturer's protocol (L3000015, Invitrogen).

For siRNA transfection, cells were transfected with 10 uM siRNA by oligofectamine reagent per the manufacturer's recommendations (12252-011, Invitrogen).

PLD3 knockout cell lines

PLD3 knockout in SH-SY5Y neuroblastoma cells was performed by Abcam as described previously. Briefly, two guiding RNAs (*PLD3*-g1: AGCCCACAACCGCCAGAATG; *PLD3*-g2: TACTCGCAAGGGTCATAGCA) were transfected into SY-SY5Y cells (CRL-2266, ATCC) individually with Cas9 gene to generate two *PLD3* knockout clones (C3 and C4). A DNA deletion (~100bp) in exon 5 of *PLD3* gene in both alleles was achieved, making the frameshift knockout. The resulting DNA deletion was subsequently confirmed by PCR and further validated at protein level by western blotting.

Western blotting

Cell lysates were prepared with RIPA buffer supplemented with complete protease inhibitors and phosphatase inhibitors as described before[24]. Protein concentration was measured using BCA protein assay kit (23227, ThermoFisher Scientific). The protein samples were then mixed with Laemmli 4x buffer and boiled for 5 minutes at 95□. Twenty to thirty micrograms of protein samples were run on SDS-PAGE gels and then transferred to PVDF membranes. The membranes were then dehydrated at 37□ for 10 minutes and soaked with methanol to enhance protein binding. Next, the membranes were washed with tris-buffered saline (TBS) and then blocked with a 5% bovine serum albumin (BSA) solution for 1 hour at room temperature. The membranes were then incubated with primary antibody diluted in a 5% BSA solution overnight at 4□. Following three washes with TBS containing 0.05% Tween 20 (TBST), the membranes were incubated with secondary antibodies diluted in TBS for 1 hour at room temperature. After three 10-minute washes with TBST, the chemiluminescent signals were revealed using Femto substrate (37074, ThermoFisher Scientific) and ChemiDoc MP Imaging System (12003154, Bio-Rad).

High content screening (HCS) microscopy

Immunofluorescence staining. Cells were seeded at a concentration of $10x10^4$ per well in pre-coated 8-well chamber slides (154941, ThermoFisher Scientific) and allowed to attach overnight.

The cells were then subjected to treatment with DMSO, dextran (0.25mg/ml), HBSS or Torin 1 (1uM) for three hours at 37□, followed by washing with PBS for 10 minutes. The cells were then fixed in ethanol containing 5% glacial acetic acid for 12 minutes at -20□. After three washes for 10 minutes each with PBS, the cells were incubated with blocking buffer containing 1% BSA, 0.5% Triton X-100, and 2% normal donkey serum for 1 hour at room temperature. The cells were then incubated with primary antibody diluted in buffer containing 1% BSA and 0.5% Triton X-100 overnight at 4□. Following three washes with PBS for 10 minutes each, the cells were incubated with secondary antibody for 1 hour at room temperature. The chambers and gaskets were then removed, and the glass slide was applied with mounting medium containing DAPI for nuclear staining. Subcellular fluorescence was detected, imaged, and analyzed using CellInsight CX7 LED Pro HCS Platform.

Lysosome labeling with dextran. For lysosome labeling with dextran, cells were seeded at the concentration of $40x10^3$ cells per well in Nunc microwell 96-well optical-bottom plates and allowed to attach overnight. The cells were then incubated with dextran Oregon Green (0.25mg/ml) and dextran Alex Fluor 594 (0.25mg/ml) overnight at 37□, followed by a chasing period of 6 hours to minimize endosome labeling. The staining medium was then removed, and the cells were incubated with neurobasal-A medium containing Hoechst for 2 hours at 37□. Subcellular fluorescence was then subjected to analysis by CellInsight CX7 LED Pro HCS Platform.

Co-localization analysis of dextran and LAMP1-RFP. Cells were seeded at the concentration of $40x10^3$ cells per well in Nunc microwell 96-well optical-bottom plates and allowed to attach overnight. A construct that expresses LAMP1-fused RFP was delivered into cells using BacMam 2.0 technology to specifically target lysosomes, following the manufacturer's protocol. On the second day, the medium was removed, and the cells were incubated with dextran Alex Fluor 647 (0.25mg/ml) overnight in the incubator, followed by a chasing period of six hours. The staining medium was then removed, and the cells were stained with Hoechst in neurobasal-A medium with clear color for 2 hours at 37□. Subcellular fluorescence was then subjected to analysis by CellInsight CX7 LED Pro HCS Platform.

Lysosomal function assay. Similarly, cells were seeded at the concentration of $40x10^3$ cells per well in Nunc microwell 96-well optical-bottom plates and allowed to attach overnight. The cells were then treated with DMSO, Torin-1 (1uM), or Bafilomycin A (100nM) for 3 hours, followed by incubation with DQ Green BSA (10 ug/ml, D12050, ThermoFisher Scientific) and Alexa Fluor 647 BSA (10 ug/ml, A34785, ThermoFisher Scientific) for 3 hours in the incubator. The assay medium was then removed, and the cells were incubated with Hoechst in neurobasal-A medium for nuclear staining for 2 hours 37°C. Subcellular fluorescence was subsequently analyzed using CellInsight CX7 LED Pro HCS Platform.

Spot detection and quantification by CellInsight CX7 LED Pro HCS platform. Subcellular fluorescence was detected and imaged in acquisition mode on the CX7 HCS platform. Images (n=30-50) per well were automatedly captured using laser autofocus, and the in-focus images were selected for subsequent analysis. For quantification analysis, images were first preprocessed with background removal, smoothing and segmentation, followed by spot (fluorescent signals) identification and validation. The spots were compartmentalized into cell body part (circle) and distal part (ring). All images were re-scanned in disk mode, and the information about spot area and intensity (total and average) on all channels was reported and statistically analyzed. Three to six independent experiments (n=3-6) were performed for final statistical analysis.

Transmission electron microscopy

Cells were fixed in 0.1 M cacodylate buffer containing 2.5% glutaraldehyde, harvested using a cell scraper and pelleted. Samples were then sequentially postfixed in 1% tannic acid and 1% OsO4, followed by en block staining in 2% uranyl acetate. After post-fixation the samples were dehydrated in a graded ethanol series and infiltrated with Quetol 651-based Spurr's resin using propylene oxide as a transition solvent. The resin was polymerized at 60 °C for 48 hours, and 70 nm sections were cut on a Leica UC7 ultramicrotome.

Imaging was performed on a JEOL 2100+ transmission electron microscope operating at 200 keV, with images captured using an AMT nanosprint CMOS camera. Single images were acquired with AMT imaging software, while tiled imaged sets were acquired using SerialEM

automation software. Tiled dataset were processed using the IMOD/etomo software suite and FIJI. Lysosome characteristics were analyzed and quantified using FIJI.

Lysosomal protein preparation

Lysosomes were isolated and purified as described previously[24]. Briefly, cells were grown to around 80% confluency and incubated with DMEM medium containing 10 mg/ml dextran-coated iron oxide nanoparticles for 8 hours. The cells were then washed three times with complete DMEM medium and rested in incubator for 16 hours. The cells were collected in homogenization buffer (containing protease inhibitors) and homogenized with Dounce homogenizer for 12 strokes. The lysates were centrifuged, and the supernatants, post-nuclear supernatant (PNS), were then passed through a pre-equilibrated column that was pre-filled with fine steel wool and embedded in a magnet. The flow-through (FT) was collected after being applied to the column three times. Next, the column was washed with homogenization buffer three times and removed from the magnet. The lysosomes fraction (LF) in the column were then eluted and lysed with buffers that are compatible with the following experiments. For Western blot analysis, RIPA buffer was used; for proteomic study, PBS containing 1% SDS was used.

Differentiation of SH-SY5Y human neuroblastoma cells

SH-SY5Y cells were differentiated into neurons following a established protocol as described[50]. Briefly, approximately $5x10^6$ neuroblastoma cells were plated in 10-cm dishes and cultured in EMEM medium supplemented with 15% FBS, 1% penicillin/streptomycin and 2mM glutamine. On the second day, cells were switched to EMEM medium containing 2.5% FBS, 1% penicillin/streptomycin, 2mM glutamine and 10uM retinoic acid (RA), with medium refreshed every three days. On day 8, cells were split and cultured in EMEM medium containing 1% FBS, 1% penicillin/streptomycin, 2mM glutamine and 10uM RA. On day 10, cells were transferred to poly-L-lysine- and laminin-coated 96-well plates or 8-well chambers and cultured in neurobasal medium containing 2% B-27, 20mM potassium chloride, 1% penicillin/streptomycin, 2 mM glutamaxl, 50ng/ml BDNF and 10uM RA, with the medium refreshed every three days. On day 18, cells were examined under a microscope to confirm their neuronal phenotype. Neuronal cultures were subsequently used for immunostaining or dextran labeling within 10 days of terminal differentiation.

Immunoprecipitation (IP)

Briefly, cells were washed with PBS and then lysed in Pierce IP lysis buffer (87787, ThermoFisher Scientific). Approximately 500 ug of lysates were pre-cleared with 0.5 ug of normal rabbit IgG and 10ul of protein G/A agarose solution, followed by incubation for 1 hour at room temperature. The supernatant was subsequently incubated overnight with 30 ul of protein G/A agarose solution and 5 ug of TFE3 antibody or rabbit normal IgG (IP control). On the following day, agarose beads were briefly centrifuged and washed three times with PBS. The agarose pellets were then reconstituted with 40 ul of 2x Laemmli protein buffer (1610747, Bio-rad), followed by Western blot analysis to detect ubiquitinated TFE3.

Isolation of cytoplasmic and nuclear proteins

Cytoplasmic and nuclear proteins were isolated from cells of interest following the instructions in the manufacturer's user guide (78833, ThermoFisher Scientific). Briefly, cells were detached with trypsin-EDTA treatment and pelleted by centrifuge at 500 xg for 5 minutes. The cells were then washed once with PBS. After the PBS wash, the cell pellet was resuspended in CER I buffer, vortexed and incubated on ice for 10 minutes. CER II buffer was then added to the suspension and mixed, followed by incubation for 1 minute. The suspension was then centrifuged, and the supernatant was immediately transferred to another tube (cytoplasmic proteins). The remaining nuclear pellet was resuspended in ice-cold NER buffer and incubated on ice for at least 40 minutes with intermittent vortexing every 10 minutes. The suspension was then centrifuged, and the supernatant was collected in a new tube (nuclear proteins). The volume ratio of CER I: CER II: NER reagents was maintained and proportional to cell numbers as instructed in the user guide.

Mass spectrometry and bioinformatic analysis

Protein samples were prepared with 5% SDS, processed using S-Trap (ProtiFi) digestion, and analyzed by LC-MS/MS, following a protocol as described previously[51]. Proteins were first reduced with 10 mM TCEP, alkylated with 20 mM iodoacetamide, and then 2.5% aqueous phosphoric acid was added, which is followed by the addition of S-Trap binding buffer (90% methanol in 100 mM TEAB) at six times the sample volume. The samples were loaded onto S-Trap microcolumns, washed with binding buffer, and digested with trypsin gold (Promega) at a

1:10 enzyme-to-protein ratio in 50 mM TEAB (pH 8.0) for 1 hour at 47°C. Peptides were eluted in series with 40 µL each of 50 mM TEAB, 0.2% formic acid, and 35 µL of 0.2% formic acid in 50% acetonitrile. The eluted peptides were dried and reconstituted in 0.1% formic acid for LC-MS/MS analysis. Peptides were loaded onto a C18 reverse-phase analytical column using a Dionex Ultimate 3000 nanoLC system with autosampler and eluted using a 90-minute gradient (1–72 min: 2–38% B; 72–78 min: 38–90% B; 78–80 min: 90% B; 80–81 min: 90–2% B; 81–90 min: 2% B for re-equilibration). The Orbitrap Exploris 240 mass spectrometer (Thermo Scientific), equipped with a nanoelectrospray ionization source, was used for data-dependent acquisition. The instrument method included MS1 scans with an MS AGC target of 3×10^6, followed by 20 MS/MS scans of the most abundant ions detected in each MS1 scan. The intensity threshold for triggering MS/MS scans was set at 1×10^4, with an MS2 AGC target of 1×10^5. Dynamic exclusion was set to 10 seconds, and HCD collision energy was 30 nce. The LC-MS/MS data were analyzed using Maxquant against a human database created from the UniprotKB protein database, with Maxquant contaminants added[52]. Standard Maxquant parameters were applied, along with LFQ and match-between-runs. Variable modifications included methionine oxidation and N-terminal acetylation, while carbamidomethyl cysteine was set as a fixed modification. A false discovery rate (FDR) of 0.01 was applied to peptide and protein identifications. Label-free quantitative (LFQ) analysis of the identified proteins was performed using the MSstats R package with default parameters[53].

RNA extraction, sequencing and bioinformatic analysis

RNA extraction. Total RNA was isolated from cells of interest using RNeasy Mini Plus Kits (74134, Qiagen) following the manufacturer's protocol, with each group having three replicates. Two micrograms of RNA per sample were submitted to Vanderbilt Technologies for Advanced Genomics (VANTAGE) for quality control analysis, library preparation and next-generation sequencing (NGS). RNA quality control was performed using the Agilent Bioanalyzer and RNA quantity was determined using the RNA Qubit assay (Q10210, ThermoFisher Scientific).

Library preparation and RNA sequencing. Library preparation was started with ribosomal RNA removal using NEBNext rRNA Depletion kit according to the manufacturer's recommendations and 500ng of input total RNA (E6310L, New England Biolabs). Following

rRNA depletion, the RNA samples were subjected to mRNA enrichment using oligo(dT) beads and subsequent fragmentation using divalent cation with elevated temperature. Libraries were generated by cDNA synthesis with random hexamer primers, RNase H digestion, A-tailing, and adapter ligation. The cDNA libraries were assessed for their quality with a Bioanalyzer and quantified using the KAPA Library Quantification Kit according to the manufacturer's recommendations (KK4824, Roche). The libraries were then mixed in equal molar ratios and the resulting library pools underwent cluster generation using the NovaSeq 6000 System according to the manufacturer's protocol. A 150 bp paired-end sequencing was performed on the NovaSeq 6000 platform, which was set to target 30M reads per sample. Real Time Analysis Software (RTA) and NovaSeq Control Software (NCS) (1.8.0; Illumina) were used for base calling. MultiQC (v1.7; Illumina) was used for data quality assessments.

Bioinformatic analysis. The raw sequencing data (FASTQ files) were subjected to quality and adapter trimming and quality control using the wrapper program, Trim Galore. The GRCh38 human transcriptome from GENCODE was used to build the transcriptome index with the program Kallisto[54]. After being processed by Trim Galore, the sequences were mapped and quantified into transcript-level abundance using the Kallisto program[54]. Transcript-level abundance was then summarized into gene-level abundance, followed by differential gene expression analysis using DESeq2 in R[55]. Heatmap representation of gene-level abundance, principal component analysis (PCA), and volcano plot representation of differentially expressed (DE) genes were all performed and graphed with R. Normalized RNA-Seq quantification was then submitted to GSEA website for gene set enrichment analysis (GSEA) with c2.cp.kegg_legacy.v2023.2.Hs.symbols.gmt as the gene set database[56].

Statistical analysis

All data were graphed and statistically analyzed using GraphPad software (version 10.0.2) or R packages unless stated otherwise. For gene set enrichment analysis, statistical tests were based on the Kolmogorov-Smirnov test[56]. For RNA-Seq differential gene expression analysis, the data were subject to negative binomial generalized linear model fitting and Wald statistics[55]. To compare between two groups, parametric unpaired *t*-test or Welch's *t*-test were used. To compare more than two independent groups, ordinary one-way ANOVA was used followed by

Tukey's or Dunnett multiple comparisons, or non-parametric Kruskal–Wallis tests were performed followed by Dunn's multiple comparisons test. To assess the individual and interaction effects of two variables, two-way ANOVA tests were performed, followed by Dunnett test. Statistical tests were specified and noted in the respective figure legends. A significant level of 0.05 was used to reject null hypothesis throughout this article unless noted otherwise.

Acknowledgments

We are very thankful to the patients who generously donated their brains for this study. We aslo acknowledge the contributions of the Vanderbilt Cell Imaging Shared Resource (CISR) Core for transmission electron microscopy, the Vanderbilt Technologies for Advanced Genomics (VANTAGE) Core for RNA sequencing, and the Mass Spectrometry Research Center for proteomic analysis. This project is financially supported by grants from the National Institutes of Health (1R56AG074279, 1K76AG060001) and a National Institutes of Health training grant (5T32AG058524).

Declaration of interests

The authors declare no competing interests.

Figure Legends

Figure 1. PLD3 deficiency alters the morphology and function of lysosomes. A, Western blot analysis of PLD3 to verify *PLD3* KO in clone 3 (KO_C3) and clone 4 (KO_C4). PLD3 was quantified, expressed relative to GAPDH, and compared between phenotypes (n=3, mean ± SEM, Kruskal–Wallis tests followed by Dunn's multiple comparisons test). **B**, Electron microscopy analysis of lysosomes in WT and *PLD3* KO cells. Scale bars, 500 nm. Lysosomal features (size, density, and confluency) were quantified and compared between WT and KO cells. For size: WT, n = 44 lysosomes; KO, n =45 lysosomes (Welch's t test). For lysosome density (count per 100 um^2): WT, n = 13 images; KO, n =12 images (Welch's t test). For lysosome confluency (occupied are): WT, n = 44 lysosomes; KO, n =45 lysosomes (Welch's t test). **C**, Dextran labeling of lysosomes in WT and KO cells overnight, followed by a chasing period of at least 6 hours and Hoechst nuclear counterstaining for 1 hour. Dextran OG (pH-sensitive) and dextran

Alexa 594 (pH-insensitive): 0.25mg/ml. Lysosomal features (size, positioning, number, total area, and endocytic activity) were assessed and compared between WT and KO cells (n=4 independent experiments, mean±SEM, unpaired t test). Scale bars, 50 µm. **D,** DQ-BSA puncta in WT and KO cells incubated with DQ-BSA (10ug/ml) and Alexa 647-BSA (10ug/ml) overnight and followed by a chasing period of at least 6 hours and Hoechst nuclear counterstaining for 1 hour. DQ intensity was normalized and compared between WT and KO cells (n=12, mean ± SEM, unpaired t test). Scale bars, 50 µm. **E**, Western blot analysis of LC3-I and LC3-II in WT and KO cells treated with Torin 1 (1uM) for 3 hours. Proteins were quantified, expressed relative to β-tubulin, and compared between phenotypes (n=3, mean ± SEM, one-way ANOVA followed by Dunnett multiple comparisons).

Figure 2. Loss of PLD3 induces lysosomal proteome remodeling. A, Lysosomes were isolated from WT and *PLD3* KO cells and verified by Western blot analysis of lysosomal proteins and β-tubulin. PNS: post-nuclear supernatant. FT: flow-through. LF: lysosome fraction. Lysosomal proteins were quantified, expressed relative to β-tubulin in PNS, and compared between WT and KO (n=3, mean ± SEM, one-way ANOVA followed by Dunnett's multiple comparison test). **B**, Proteomic analysis of the lysosomal lysates from WT and KO cells (clone 3). The differentially expressed proteins were represented by heatmap (n=3, ≥1.5-fold change, false discover rate (FDR) < 0.05). **C**, Proteomic data (normalized) were subject to GSEA analysis, and the differentially regulated pathways in KO versus WT were summarized and represented by bar plots (FDR q value < 0.05). **D**, GSEA plots featuring upregulated endosomal, and lysosomal pathways in *PLD3* KO versus WT (FDR q-value < 0.05; nominal p-value <0.05). **E**, Lysosomal proteins from proteomic analysis were quantified and compared between WT and KO, and the differentially regulated proteins were represented by bar graphs (mean ± SEM, multiple unpaired t test).

Figure 3. PLD3 regulates TFEB/TFE3 metabolism. A, Western blot analysis of TFEB, TFE3 and PLD3 in WT and KO cells treated with vehicle (NS), dextran (0.25mg/ml), HBSS, or Torin 1 (1uM) for 3 hours. NS: non-stimulation. Proteins were quantified, expressed relative to β-tubulin, and compared between genotypes (n=3-4, mean ± SEM, two-way ANOVA followed by Dunnett's multiple comparison test). **B**, Western blot analysis of TFEB and PLD3 in WT and

KO cells transfected with control plasmids (CTL-P) or GFP-tagged TFEB plasmids (GFP-N-TFEB) for 2 days. TFEB and PLD3 were quantified, expressed relative to β-tubulin, and compared between genotypes (n=3-4, mean ± SEM, two-way ANOVA followed by Dunnett's multiple comparison test). **C**, Western blot analysis of TFEB, TFE3 and PLD3 in HeLa cells transfected with control plasmids (CTL_P) or *PLD3* plasmids for 2 days. Proteins were quantified, expressed relative to β-tubulin, and compared between genotypes (n=3-4, mean ± SEM, one-way ANOVA followed by Dunnett's multiple comparison test).

Figure 4. Proteasomes, rather than lysosomes, are involved in PLD3-mediated TFEB/TFE3 metabolism. A-C, Western blot analysis of TFEB, TFE3 and PLD3 in WT and KO cells treated with MG132 (1uM) for 4 hours (**A**), 8 hours (**B**), and 16 hours (**C**). Proteins were quantified, expressed relative to β-tubulin, and compared among experimental conditions (n=3-4, mean ± SEM, two-way ANOVA followed by Dunnett's multiple comparison test). **D**, Western blot analysis of TFEB, TFE3 and PLD3 in WT and KO cells treated with cycloheximide (CHX, 20 ug/mL) and/or MG132 (1 uM) for 4 hours (representative images of two independent experiments). **E**, Western blot analysis of TFE3 immunoprecipitation for TFE3 and ubiquitin from the lysates of WT and KO cells treated with or without MG132 (1uM) for 4 hours. An immunoprecipitation control with rabbit normal IgG was included to demonstrate the specificity of the immunoprecipitation (representative images of two independent experiments). **F-G**, Western blot analysis of TFEB, TFE3 and PLD3 in WT and KO cells treated with bafilomycin A1 (BafA1, 200 nM) or chloroquine (CQ, 50 uM) for 6 hours and 24 hours. Proteins were quantified, expressed relative to β-tubulin, and compared among experimental conditions (n=3-4, mean ± SEM, two-way ANOVA followed Dunnett's multiple comparison test).

Figure 5. Loss of PLD3 augments TFEB/TFE3 nuclear localization transcriptional activities. A, Western blot analysis of TFEB, TFE3 and PLD3 in nuclear and cytoplasmic fractions of WT and KO cells treated with HBSS (vs NS), or 1uM Torin 1 (vs DMSO) for 3 hours. NE: nuclear extract; CE: cytoplasmic extract. Proteins were quantified and normalized to GAPDH or Lamnin B1. Proteins in NE or their NE-to-CE ratios were compared among experimental conditions (n=3-4, mean ± SEM, two-way ANOVA followed by Dunnett's multiple comparison test). **B**, Immunostaining of TFEB (green) in WT and KO cells treated with

HBSS (vs NS) or 1 uM Torin 1 (vs DMSO) for 3 hours with DAPI nuclear counterstaining (blue). Scale bars, 50 µm. NS: non-stimulation. TFEB was quantified and compared among experimental conditions in one representative experiment out of three-independent experiments (n=20-25 fields, mean ± SEM, two-way ANOVA followed by Dunnett's multiple comparison test). **C**, **D**, Transcript levels of genes containing CLEAR motif (**C**) or genes responsive to TFEB (**D**) in WT and KO cells were calculated and compared between WT (n=3) and KO (n=3). mean ± SEM, multiple unpaired *t* test.

Figure 6. *PLD3* knockdown causes enrichment in lysosome-related signaling. A, RNA-Seq data were subject to gene set enrichment analysis (GSEA), and the differentially enriched pathways in *PLD3*_siRNAs (n=9) versus CTL_siRNA were summarized and represented by bar plots (FDR q value < 0.05). **B**, GSEA plots featuring upregulated endosomal, autophagic and lysosomal pathways in *PLD3*_siRNAs versus CTRL_siRNA (FDR q-value < 0.15; nominal p-value <0.05). **C**, RNA expression in genes related to the lysosome pathway was calculated and compared between CTL_siRNA (n=3) and *PLD3*_siRNAs (n=9), and significantly different genes were represented by bar graphs (mean ± SEM, multiple unpaired t test). **D**, RNA expression in genes related to AD was calculated and compared between CTL_siRNA (n=3) and *PLD3*_siRNAs (n=9), and significantly different genes were represented by heatmap (mean ± SEM, multiple unpaired t test).

Figure 7. Loss of PLD3 intensifies amyloid-induced lysosomal abnormalities and TFEB signaling. A, Dextran labeling of lysosomes in neuroblastoma-derived neurons treated with CAA patients-derived Aβ seeds (100 ng/ml) for 1 day, 3 days and 5 days. Quantification, and comparison of lysosome features (size, positioning, number, total area, and alkalinization) among experimental conditions (n= 5-6, mean ± SEM, one-way ANOVA followed by Dunnett's multiple comparison test). Scale bars, 500nm. NS: non-stimulation. **B**, Western blot analysis of TFEB, TFE3 and PLD3 in WT and KO neuroblastoma cells treated with synthetic Aβ1-42 (1 ug/ml) for 1, 3, 5, and 7 days. Proteins were quantified, expressed relative to β-tubulin, and compared among experimental conditions (n=3-4, mean ± SEM, two-way ANOVA followed by Dunnett's multiple comparison test). **C**, Western blot analysis of TFEB, TFE3 and PLD3 in non-AD and AD brain gray matter (n=7-10, mean ± SEM, unpaired t test).

Supplementary Figure 1. Co-localizations of dextran and Lyso-RFP. Dextran (green) and Lyso-RFP (red) were analyzed in WT and KO cells transduced with Lyso-RFP viruses for 24 hours and then stained with dextran Alexa 647 overnight, followed by a chasing period of at least 6 hours and Hoechst nuclear counterstaining for 2 hours. Scale bars, 10 µm. Colocalization/correlation of dextran and lyso-RFP was assessed by Pearson coefficient and Mander's coefficient and compared between WT and KO (n=3, unpaired t test).

Supplementary Figure 2. Proteomic analysis of lysosomal proteins isolated from PLD3 KO clone 4. A, Proteomic analysis of the lysosomal lysates from WT and KO cells (clone 4). The differentially expressed proteins were represented by heatmap (n=3, ≥1.5-fold change, false discover rate (FDR) < 0.05). **B**, Proteomic data (normalized) were subject to GSEA analysis, and the differentially regulated pathways in KO versus WT were summarized and represented by bar plots (FDR q value < 0.05). **C**, GSEA plots featuring the enriched lysosomal pathway in *PLD3* KO versus WT (FDR q-value < 0.05; nominal p-value <0.05). **D**, Lysosomal proteins from proteomic analysis were quantified and compared between WT and KO, and the differentially regulated proteins were represented by bar graphs (mean ± SEM, multiple unpaired t test).

Supplementary Figure 3. PLD3 modulates TFEB/TFE3 metabolism without affecting their transcription. A, RNA levels of TFEB and TFE3 from RNA sequencing of total RNA in WT and *PLD3* KO cells, or CTL_siRNA and *PLD3*_siRNA cells, were quantified and expressed relative to the corresponding controls (n=3, mean ± SEM, t-test). **B**, Western blot analysis of TFEB, TFE3 and PLD3 in WT and KO cells treated with vehicle (NS), dextran (0.25mg/ml), HBSS, or Torin 1 (1uM) for 8 hours. NS: non-stimulation. Proteins were quantified, expressed relative to β-tubulin, and compared between genotypes (n=3-4, mean ± SEM, two-way ANOVA followed by multiple comparison test). **C**, Western blot analysis of TFEB, TFE3 and PLD3 in WT cells transfected with control siRNAs (CTL_siRNA) or *PLD3* siRNAs for 2 days. Proteins were quantified, expressed relative to β-tubulin, and compared between genotypes (n=3-4, mean ± SEM, one-way ANOVA followed by Dunnett's multiple comparison test). **D**, Western blot analysis of p-TFEB (Ser 211) and p-TFEB (Ser 142) in WT and KO cells treated with vehicle (NS), dextran (0.25mg/ml), HBSS, or Torin 1 (1uM) for 8 hours.

Supplementary Figure 4. PLD3 mediates TFEB/TFE3 degradation through proteasomes. A, B, Western blot analysis of TFEB, TFE3 and PLD3 in WT and KO cells treated with bortezomib (BZ, 200nM/DMSO) for 4 hours (**A**) and 8 hours (**B**). Proteins were quantified, expressed relative to β-tubulin, and compared among experimental conditions (n=3-4, mean ± SEM, two-way ANOVA followed by Dunnett's multiple comparison test). **C**, Western blot analysis of IKKβ in WT and KO cells treated with BZ (200nM) or MG132 (1uM) for 4 hours. Proteins were quantified, expressed relative to β-tubulin, and compared among experimental conditions (n=3-4, mean ± SEM, two-way ANOVA followed by Tukey test). **D**, Western blot analysis of p-IKK □/β (Ser 176/180) in WT and KO cells treated with DMSO, BZ, and MG132 for 8 hours.

Supplementary Figure 5. LD3 deficiency leads to increased nuclear translocation and transcriptional activity of TFEB/TFE3. A, GFP-TFEB (green) expression in WT and KO cells transfected with GFP-N-TFEB DNA for 2 days and then treated with 1 uM Torin 1 (vs DMSO) for 3 hours with DAPI nuclear counterstaining (blue). Scale bars, 40 µm. NS: non-stimulation. Data shown are from one representative experiment out of two independent experiments. **B, C,** RNA levels of coordinated-lysosomal-expression-and-regulation (CLEAR) motif-containing genes **(B)** or TFEB responsive genes **(C)** from RNA sequencing of total RNA in CTL_siRNA and *PLD3*_siRNA cells were quantified and expressed relative to respective controls (n=3, mean ± SEM, t-test).

Supplementary Figure 6. Transcriptomic profiling following *PLD3* knockout in SY-SY5Ycells. A, RNA sequencing analysis of total RNA from WT and *PLD3* KO SH-SY5Y cells. RNA count data were log-transformed (loge) and analyzed using principal component analysis (PCA). **B**, The differentially expressed genes in *PLD3* KO cells (versus WT cells) were represented by heatmap (n=3, false discover rate (FDR) < 0.05). **C**, The differentially expressed genes were represented by volcano plots with the differentially expressed lysosomal proteins labeled. **D**, RNA-Seq data were subject to GSEA analysis, and the differentially enriched pathways were represented by bar plots. **E**, GSEA plots featuring the upregulated lysosomal pathway and AD in *PLD3* KO versus WT cells. **F**, RNA expression in genes related to the lysosome pathway was calculated and compared between *PLD3* KO (n=3) and WT (n=3), and

significantly different genes were represented by bar graphs (mean ± SEM, multiple unpaired t test).

Supplementary Figure 7. Transcriptomic profiling after *PLD3* knockdown. A, Western blot analysis of PLD3 in neuroblastoma cells transfected with CTL_siRNA or *PLD3*_siRNAs for 2 days. Proteins were quantified, expressed relative to GAPDH, and compared (n=3-4, mean ± SEM, one-way ANOVA followed by Dunnett's multiple comparison test). **B**, RNA sequencing analysis of the total RNA in neuroblastoma cells transfected with CTL_siRNA or *PLD3*_siRNAs for 2 days. The differentially expressed genes were represented by heatmap (n=3, ≥1.5-fold change, FDR < 0.05). **C**, The differentially expressed genes in cells transfected with *PLD3* siRNAs versus CTL siRNA were represented by volcano plots with lysosomal proteins labeled. **D**, RNA sequencing count data ere log-transformed (loge) and analyzed using principal component analysis (PCA).

Supplementary Figure 8. *PLD3* KO does not alter neuronal differentiation of SH-SY5Y cells. A, Morphological assessment of neuronal differentiation in WT and PLD3 KO cells.). Scale bars, 500nm. **B**, RNA sequencing analysis of total RNA from WT and *PLD3* KO cells under both undifferentiated and differentiated conditions. RNA count data were log-transformed (loge) and analyzed using principal component analysis (PCA).

References

1 Ballabio, A. & Bonifacino, J. S. Lysosomes as dynamic regulators of cell and organismal homeostasis. *Nat Rev Mol Cell Biol* **21**, 101-118 (2020). https://doi.org/10.1038/s41580-019-0185-4

2 Trivedi, P. C., Bartlett, J. J. & Pulinilkunnil, T. Lysosomal Biology and Function: Modern View of Cellular Debris Bin. *Cells* **9** (2020). https://doi.org/10.3390/cells9051131

3 Winckler, B. *et al.* The Endolysosomal System and Proteostasis: From Development to Degeneration. *J Neurosci* **38**, 9364-9374 (2018). https://doi.org/10.1523/JNEUROSCI.1665-18.2018

4 Wallings, R. L., Humble, S. W., Ward, M. E. & Wade-Martins, R. Lysosomal Dysfunction at the Centre of Parkinson's Disease and Frontotemporal Dementia/Amyotrophic Lateral Sclerosis. *Trends Neurosci* **42**, 899-912 (2019). https://doi.org/10.1016/j.tins.2019.10.002

5 Zhang, W. *et al.* Impairment of the autophagy-lysosomal pathway in Alzheimer's diseases: Pathogenic mechanisms and therapeutic potential. *Acta Pharm Sin B* **12**, 1019-1040 (2022). https://doi.org/10.1016/j.apsb.2022.01.008

6 Nixon, R. A. The role of autophagy in neurodegenerative disease. *Nat Med* **19**, 983-997 (2013). https://doi.org/10.1038/nm.3232

7 Cataldo, A. M. *et al.* Endocytic pathway abnormalities precede amyloid beta deposition in sporadic Alzheimer's disease and Down syndrome: differential effects of APOE genotype and presenilin mutations. *Am J Pathol* **157**, 277-286 (2000). https://doi.org/10.1016/s0002-9440(10)64538-5

8 Small, S. A. & Petsko, G. A. Endosomal recycling reconciles the Alzheimer's disease paradox. *Sci Transl Med* **12** (2020). https://doi.org/10.1126/scitranslmed.abb1717

9 Jucker, M. & Walker, L. C. Alzheimer's disease: From immunotherapy to immunoprevention. *Cell* **186**, 4260-4270 (2023). https://doi.org/10.1016/j.cell.2023.08.021

10 Choy, R. W., Cheng, Z. & Schekman, R. Amyloid precursor protein (APP) traffics from the cell surface via endosomes for amyloid beta (Abeta) production in the trans-Golgi network. *Proc Natl Acad Sci U S A* **109**, E2077-2082 (2012). https://doi.org/10.1073/pnas.1208635109

11 Sasanian, N., Bernson, D., Horvath, I., Wittung-Stafshede, P. & Esbjorner, E. K. Redox-Dependent Copper Ion Modulation of Amyloid-beta (1-42) Aggregation In Vitro. *Biomolecules* **10** (2020). https://doi.org/10.3390/biom10060924

12 Lee, J. H. *et al.* Faulty autolysosome acidification in Alzheimer's disease mouse models induces autophagic build-up of Abeta in neurons, yielding senile plaques. *Nat Neurosci* **25**, 688-701 (2022). https://doi.org/10.1038/s41593-022-01084-8

13 Van Acker, Z. P. *et al.* Phospholipase D3 degrades mitochondrial DNA to regulate nucleotide signaling and APP metabolism. *Nat Commun* **14**, 2847 (2023). https://doi.org/10.1038/s41467-023-38501-w

14 Mawuenyega, K. G. *et al.* Decreased clearance of CNS beta-amyloid in Alzheimer's disease. *Science* **330**, 1774 (2010). https://doi.org/10.1126/science.1197623

15 Behl, T. *et al.* The Interplay of ABC Transporters in Abeta Translocation and Cholesterol Metabolism: Implicating Their Roles in Alzheimer's Disease. *Mol Neurobiol* **58**, 1564-1582 (2021). https://doi.org/10.1007/s12035-020-02211-x

16 Wang, Y. J., Zhou, H. D. & Zhou, X. F. Clearance of amyloid-beta in Alzheimer's disease: progress, problems and perspectives. *Drug Discov Today* **11**, 931-938 (2006). https://doi.org/10.1016/j.drudis.2006.08.004

17 Hou, J., Chen, Y., Grajales-Reyes, G. & Colonna, M. TREM2 dependent and independent functions of microglia in Alzheimer's disease. *Mol Neurodegener* **17**, 84 (2022). https://doi.org/10.1186/s13024-022-00588-y

18 Pedersen, K. M., Finsen, B., Celis, J. E. & Jensen, N. A. Expression of a novel murine phospholipase D homolog coincides with late neuronal development in the forebrain. *J Biol Chem* **273**, 31494-31504 (1998). https://doi.org/10.1074/jbc.273.47.31494

19 Gonzalez, A. C. *et al.* Unconventional Trafficking of Mammalian Phospholipase D3 to Lysosomes. *Cell Rep* **22**, 1040-1053 (2018). https://doi.org/10.1016/j.celrep.2017.12.100

20 Singh, S. *et al.* PLD3 and PLD4 synthesize S,S-BMP, a key phospholipid enabling lipid degradation in lysosomes. *bioRxiv* (2024). https://doi.org/10.1101/2024.03.21.586175

21 Gonzalez, A. C. *et al.* PLD3 and spinocerebellar ataxia. *Brain* **141**, e78 (2018). https://doi.org/10.1093/brain/awy258
22 Nibbeling, E. A. R. *et al.* Exome sequencing and network analysis identifies shared mechanisms underlying spinocerebellar ataxia. *Brain* **140**, 2860-2878 (2017). https://doi.org/10.1093/brain/awx251
23 Yuan, P. *et al.* PLD3 affects axonal spheroids and network defects in Alzheimer's disease. *Nature* **612**, 328-337 (2022). https://doi.org/10.1038/s41586-022-05491-6
24 Nackenoff, A. G. *et al.* PLD3 is a neuronal lysosomal phospholipase D associated with beta-amyloid plaques and cognitive function in Alzheimer's disease. *PLoS Genet* **17**, e1009406 (2021). https://doi.org/10.1371/journal.pgen.1009406
25 Gavin, A. L. *et al.* Cleavage of DNA and RNA by PLD3 and PLD4 limits autoinflammatory triggering by multiple sensors. *Nat Commun* **12**, 5874 (2021). https://doi.org/10.1038/s41467-021-26150-w
26 Cruchaga, C. *et al.* Rare coding variants in the phospholipase D3 gene confer risk for Alzheimer's disease. *Nature* **505**, 550-554 (2014). https://doi.org/10.1038/nature12825
27 Fazzari, P. *et al.* PLD3 gene and processing of APP. *Nature* **541**, E1-E2 (2017). https://doi.org/10.1038/nature21030
28 Settembre, C. *et al.* TFEB links autophagy to lysosomal biogenesis. *Science* **332**, 1429-1433 (2011). https://doi.org/10.1126/science.1204592
29 Medina, D. L. *et al.* Lysosomal calcium signalling regulates autophagy through calcineurin and TFEB. *Nat Cell Biol* **17**, 288-299 (2015). https://doi.org/10.1038/ncb3114
30 Raben, N. & Puertollano, R. TFEB and TFE3: Linking Lysosomes to Cellular Adaptation to Stress. *Annu Rev Cell Dev Biol* **32**, 255-278 (2016). https://doi.org/10.1146/annurev-cellbio-111315-125407
31 Sha, Y., Rao, L., Settembre, C., Ballabio, A. & Eissa, N. T. STUB1 regulates TFEB-induced autophagy-lysosome pathway. *EMBO J* **36**, 2544-2552 (2017). https://doi.org/10.15252/embj.201796699
32 Xiong, Y. *et al.* (2023). https://doi.org/10.1101/2023.10.16.562572
33 Lysosome regulation of microglia in Alzheimer's disease via TFEB-vacuolar ATPase. *Nat Neurosci* **27**, 13-14 (2024). https://doi.org/10.1038/s41593-023-01495-1
34 Sardiello, M. *et al.* A gene network regulating lysosomal biogenesis and function. *Science* **325**, 473-477 (2009). https://doi.org/10.1126/science.1174447
35 Hampel, H. *et al.* The Amyloid-beta Pathway in Alzheimer's Disease. *Mol Psychiatry* **26**, 5481-5503 (2021). https://doi.org/10.1038/s41380-021-01249-0
36 Martina, J. A., Diab, H. I., Brady, O. A. & Puertollano, R. TFEB and TFE3 are novel components of the integrated stress response. *EMBO J* **35**, 479-495 (2016). https://doi.org/10.15252/embj.201593428
37 Martina, J. A. *et al.* The nutrient-responsive transcription factor TFE3 promotes autophagy, lysosomal biogenesis, and clearance of cellular debris. *Sci Signal* **7**, ra9 (2014). https://doi.org/10.1126/scisignal.2004754
38 Yang, M. *et al.* Emerging roles and regulation of MiT/TFE transcriptional factors. *Cell Commun Signal* **16**, 31 (2018). https://doi.org/10.1186/s12964-018-0242-1
39 La Spina, M. *et al.* MiT/TFE Family of Transcription Factors: An Evolutionary Perspective. *Front Cell Dev Biol* **8**, 609683 (2020). https://doi.org/10.3389/fcell.2020.609683

40 Kwart, D. *et al*. A Large Panel of Isogenic APP and PSEN1 Mutant Human iPSC Neurons Reveals Shared Endosomal Abnormalities Mediated by APP beta-CTFs, Not Abeta. *Neuron* **104**, 1022 (2019). https://doi.org/10.1016/j.neuron.2019.11.010
41 Nuriel, T. *et al*. The Endosomal-Lysosomal Pathway Is Dysregulated by APOE4 Expression in Vivo. *Front Neurosci* **11**, 702 (2017). https://doi.org/10.3389/fnins.2017.00702
42 Van Acker, Z. P., Bretou, M. & Annaert, W. Endo-lysosomal dysregulations and late-onset Alzheimer's disease: impact of genetic risk factors. *Mol Neurodegener* **14**, 20 (2019). https://doi.org/10.1186/s13024-019-0323-7
43 Jansen, I. E. *et al*. Genome-wide meta-analysis identifies new loci and functional pathways influencing Alzheimer's disease risk. *Nat Genet* **51**, 404-413 (2019). https://doi.org/10.1038/s41588-018-0311-9
44 Vaz-Silva, J. *et al*. Endolysosomal degradation of Tau and its role in glucocorticoid-driven hippocampal malfunction. *EMBO J* **37** (2018). https://doi.org/10.15252/embj.201899084
45 Terzioglu, G. & Young-Pearse, T. L. Microglial function, INPP5D/SHIP1 signaling, and NLRP3 inflammasome activation: implications for Alzheimer's disease. *Mol Neurodegener* **18**, 89 (2023). https://doi.org/10.1186/s13024-023-00674-9
46 Hansen, D. V., Hanson, J. E. & Sheng, M. Microglia in Alzheimer's disease. *J Cell Biol* **217**, 459-472 (2018). https://doi.org/10.1083/jcb.201709069
47 Sala Frigerio, C. *et al*. The Major Risk Factors for Alzheimer's Disease: Age, Sex, and Genes Modulate the Microglia Response to Abeta Plaques. *Cell Rep* **27**, 1293-1306 e1296 (2019). https://doi.org/10.1016/j.celrep.2019.03.099
48 Sobue, A. *et al*. Microglial gene signature reveals loss of homeostatic microglia associated with neurodegeneration of Alzheimer's disease. *Acta Neuropathol Commun* **9**, 1 (2021). https://doi.org/10.1186/s40478-020-01099-x
49 Gavin, A. L. *et al*. PLD3 and PLD4 are single-stranded acid exonucleases that regulate endosomal nucleic-acid sensing. *Nat Immunol* **19**, 942-953 (2018). https://doi.org/10.1038/s41590-018-0179-y
50 Shipley, M. M., Mangold, C. A. & Szpara, M. L. Differentiation of the SH-SY5Y Human Neuroblastoma Cell Line. *J Vis Exp*, 53193 (2016). https://doi.org/10.3791/53193
51 Howard, G. C. *et al*. Ribosome subunit attrition and activation of the p53-MDM4 axis dominate the response of MLL-rearranged cancer cells to WDR5 WIN site inhibition. *Elife* **12** (2024). https://doi.org/10.7554/eLife.90683
52 Cox, J. *et al*. Accurate proteome-wide label-free quantification by delayed normalization and maximal peptide ratio extraction, termed MaxLFQ. *Mol Cell Proteomics* **13**, 2513-2526 (2014). https://doi.org/10.1074/mcp.M113.031591
53 Choi, M. *et al*. MSstats: an R package for statistical analysis of quantitative mass spectrometry-based proteomic experiments. *Bioinformatics* **30**, 2524-2526 (2014). https://doi.org/10.1093/bioinformatics/btu305
54 Bray, N. L., Pimentel, H., Melsted, P. & Pachter, L. Near-optimal probabilistic RNA-seq quantification. *Nat Biotechnol* **34**, 525-527 (2016). https://doi.org/10.1038/nbt.3519
55 Love, M. I., Huber, W. & Anders, S. Moderated estimation of fold change and dispersion for RNA-seq data with DESeq2. *Genome Biol* **15**, 550 (2014). https://doi.org/10.1186/s13059-014-0550-8

56 Subramanian, A. *et al.* Gene set enrichment analysis: a knowledge-based approach for interpreting genome-wide expression profiles. *Proc Natl Acad Sci U S A* **102**, 15545-15550 (2005). https://doi.org/10.1073/pnas.0506580102

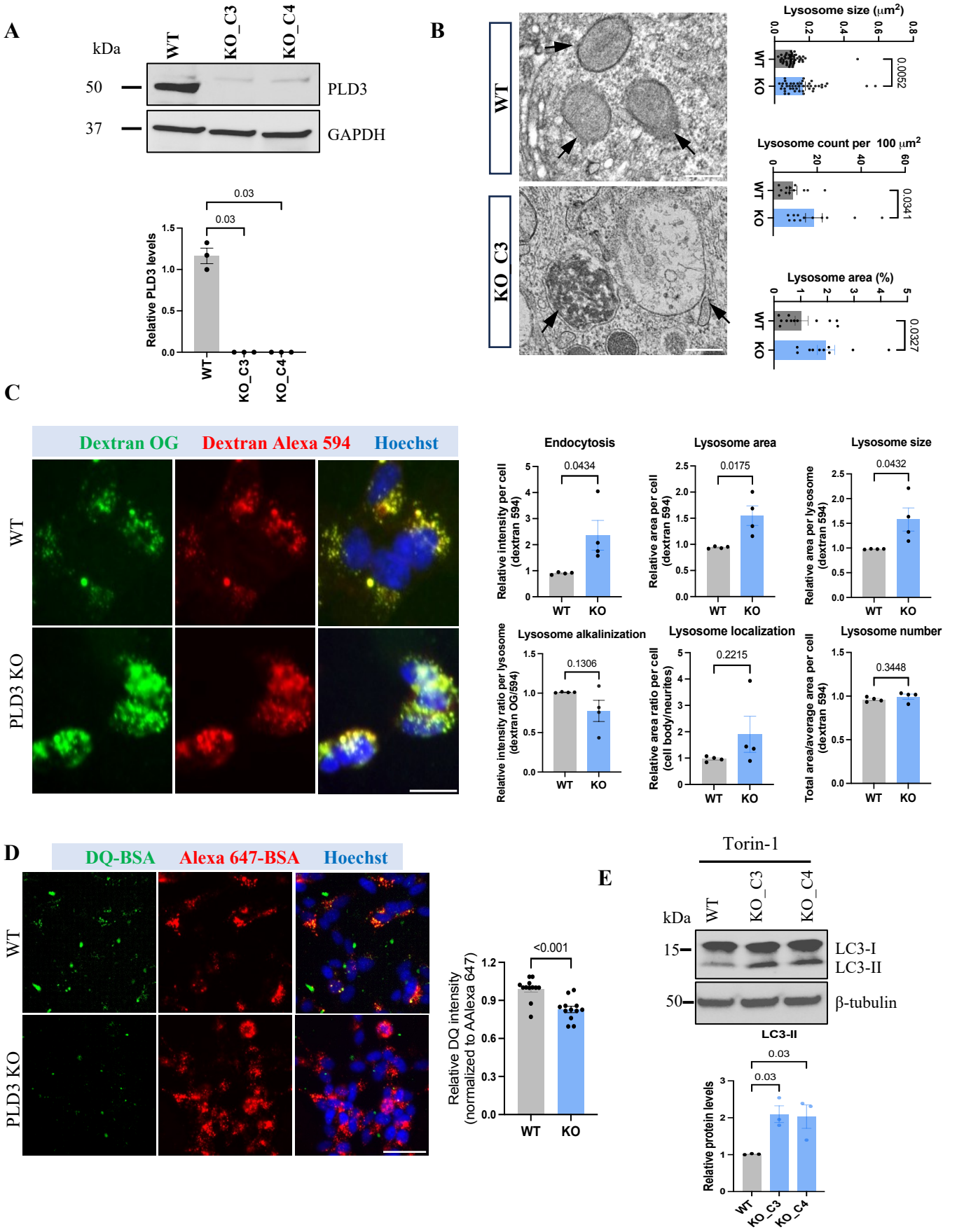

Fig 1. Loss of PLD3 alters lysosomal homeostasis and function.

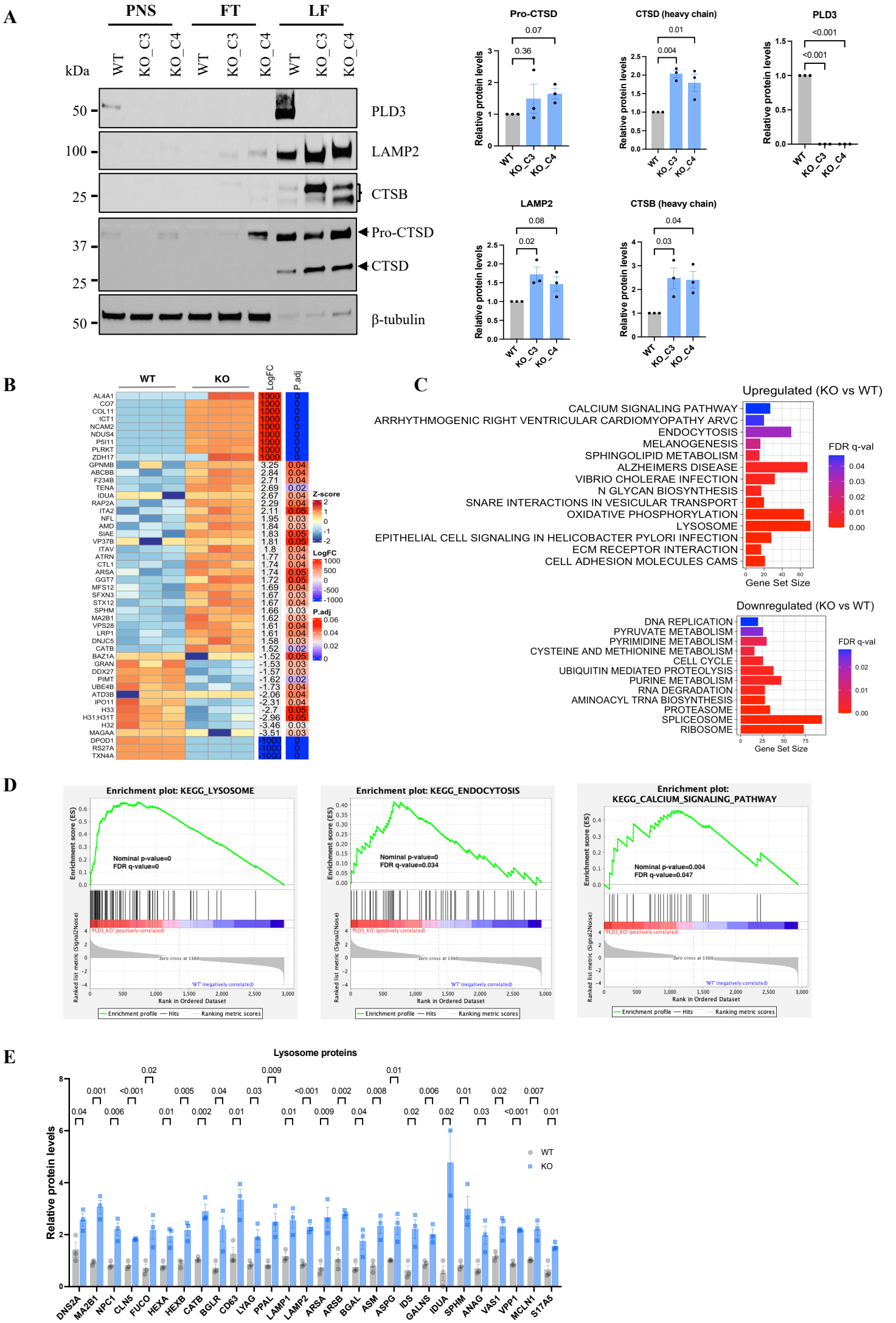

Fig 2. Loss of PLD3 causes remodeling of lysosomal proteome.

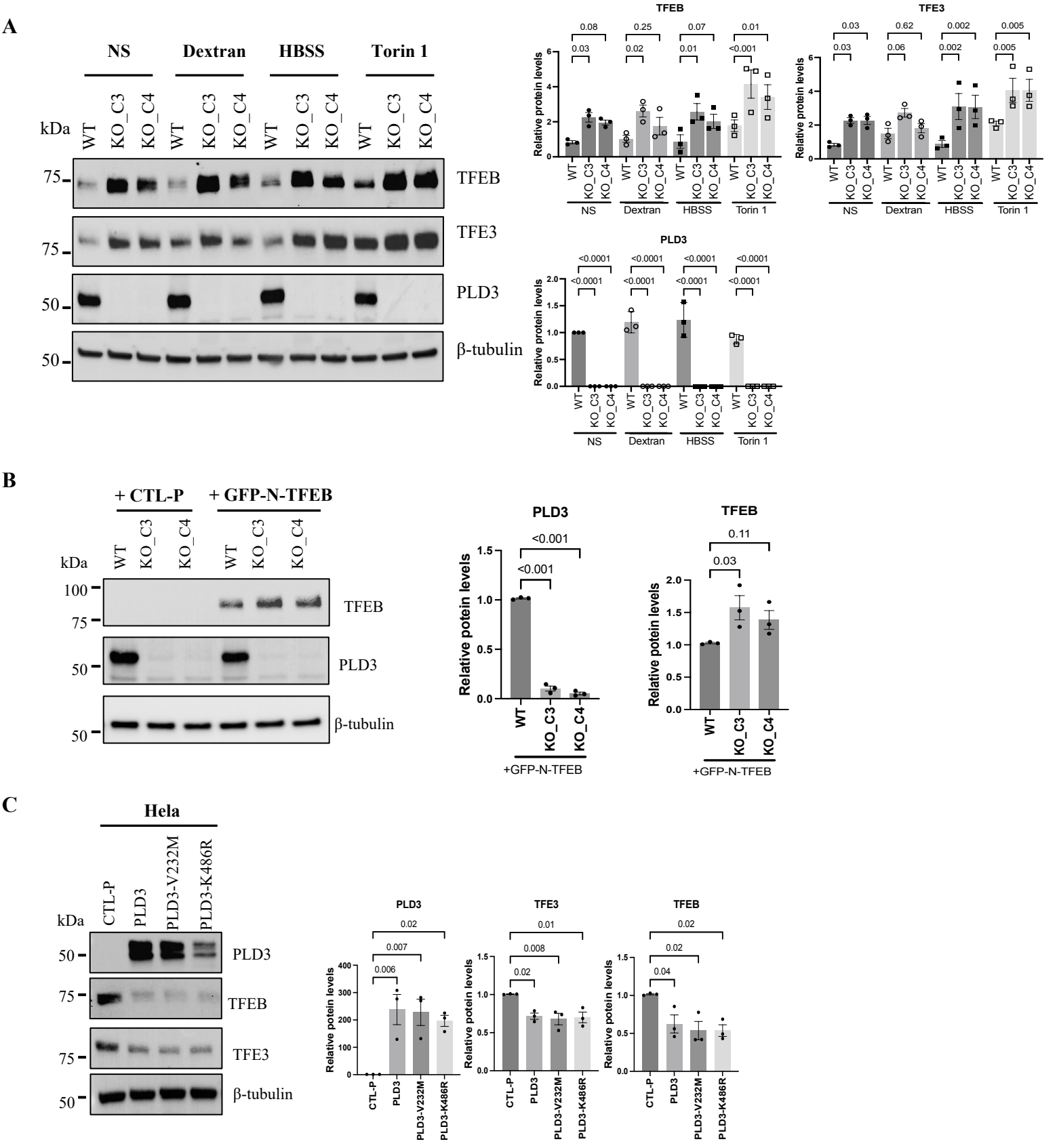

Fig 3. PLD3 modulates the metabolism of TFEB/TFE3.

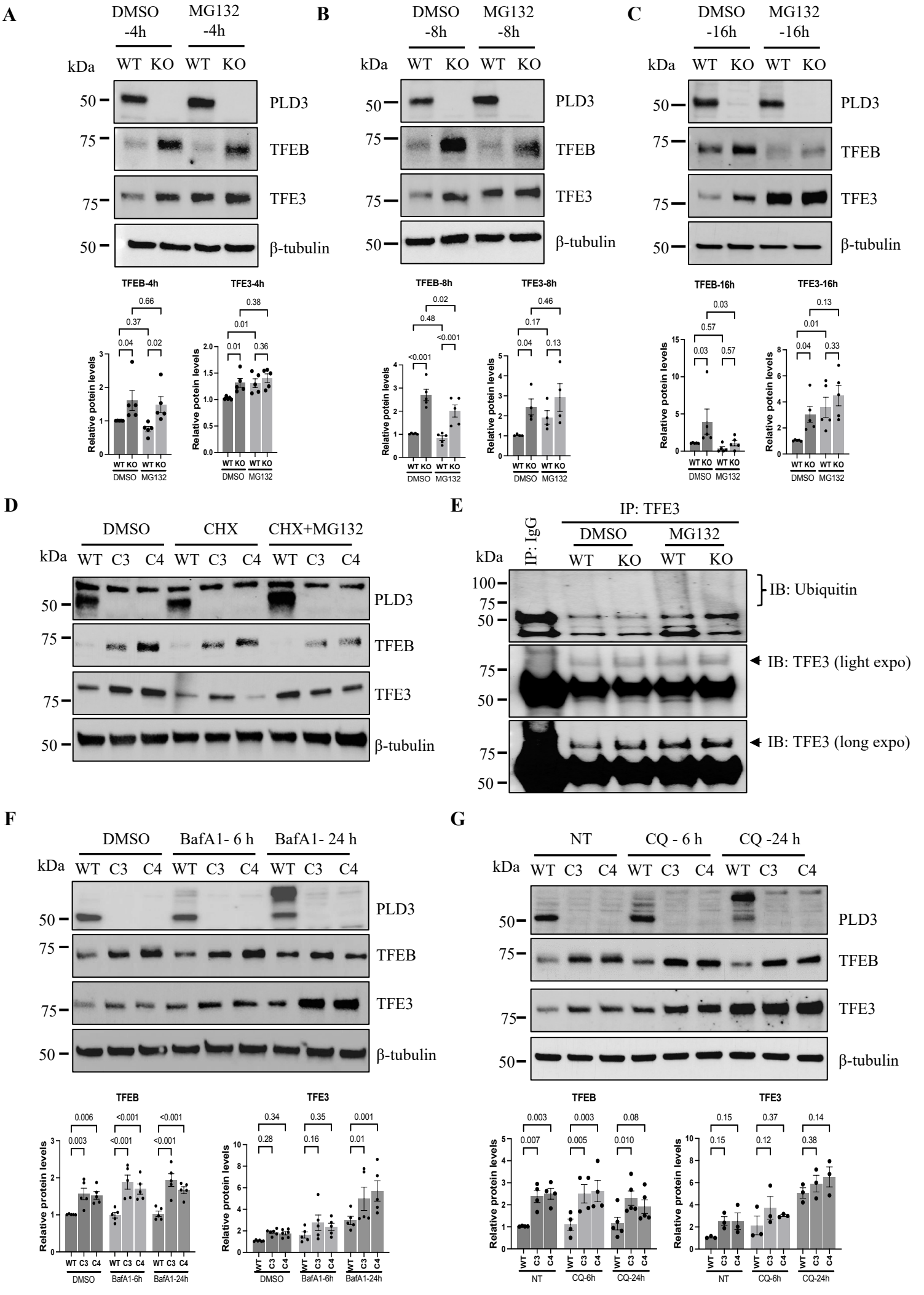

Fig 4. Proteasomes, rather than lysosomes, are involved in the metabolism of TFEB/TFE3.

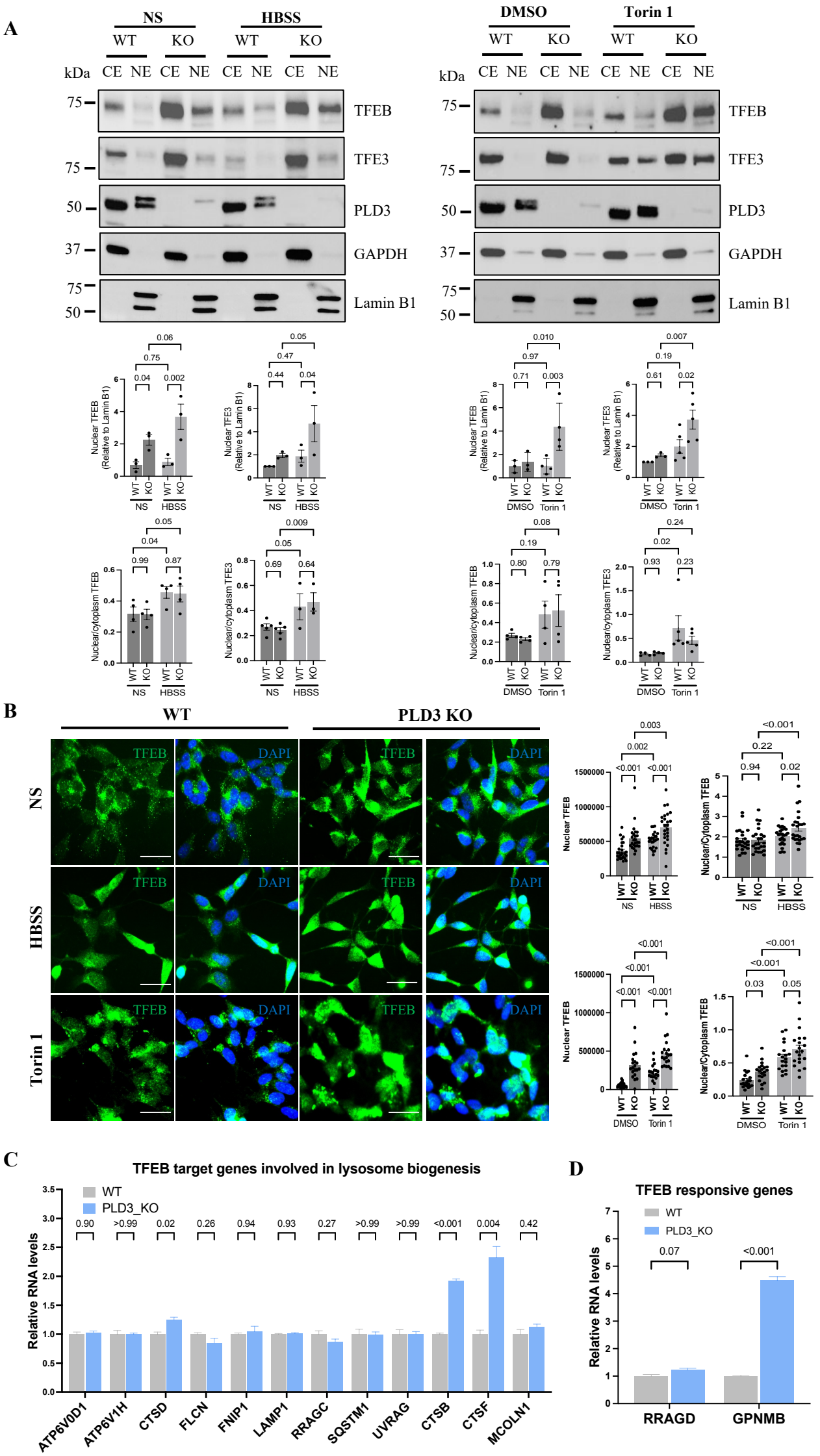

Fig 5. Loss of PLD3 increases the nuclear translocation and transcriptional activity of TFEB/TFE3.

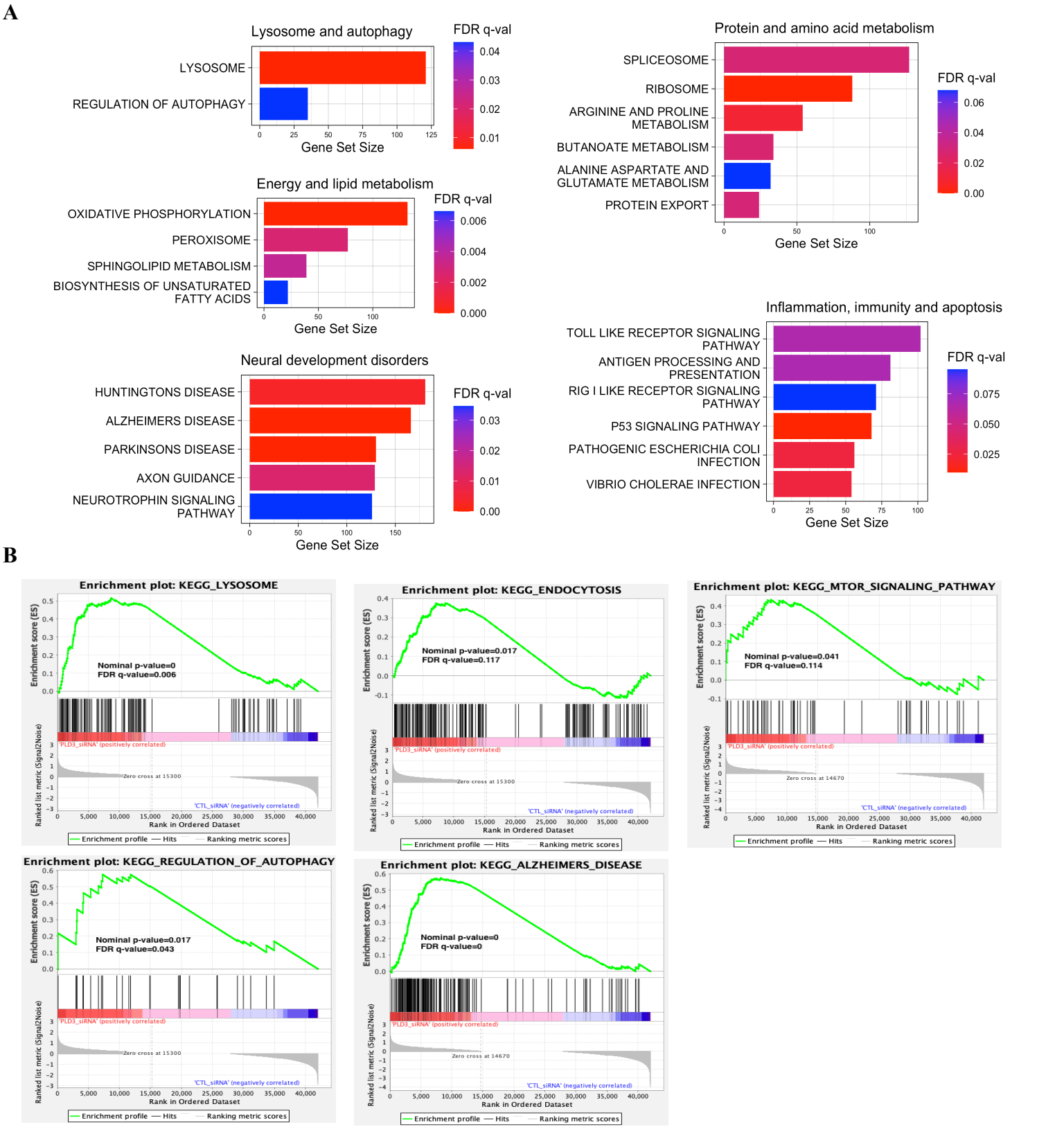

Fig 6. PLD3 knockdown enhances signaling pathways related to lysosomes and Alzheimer' disease .

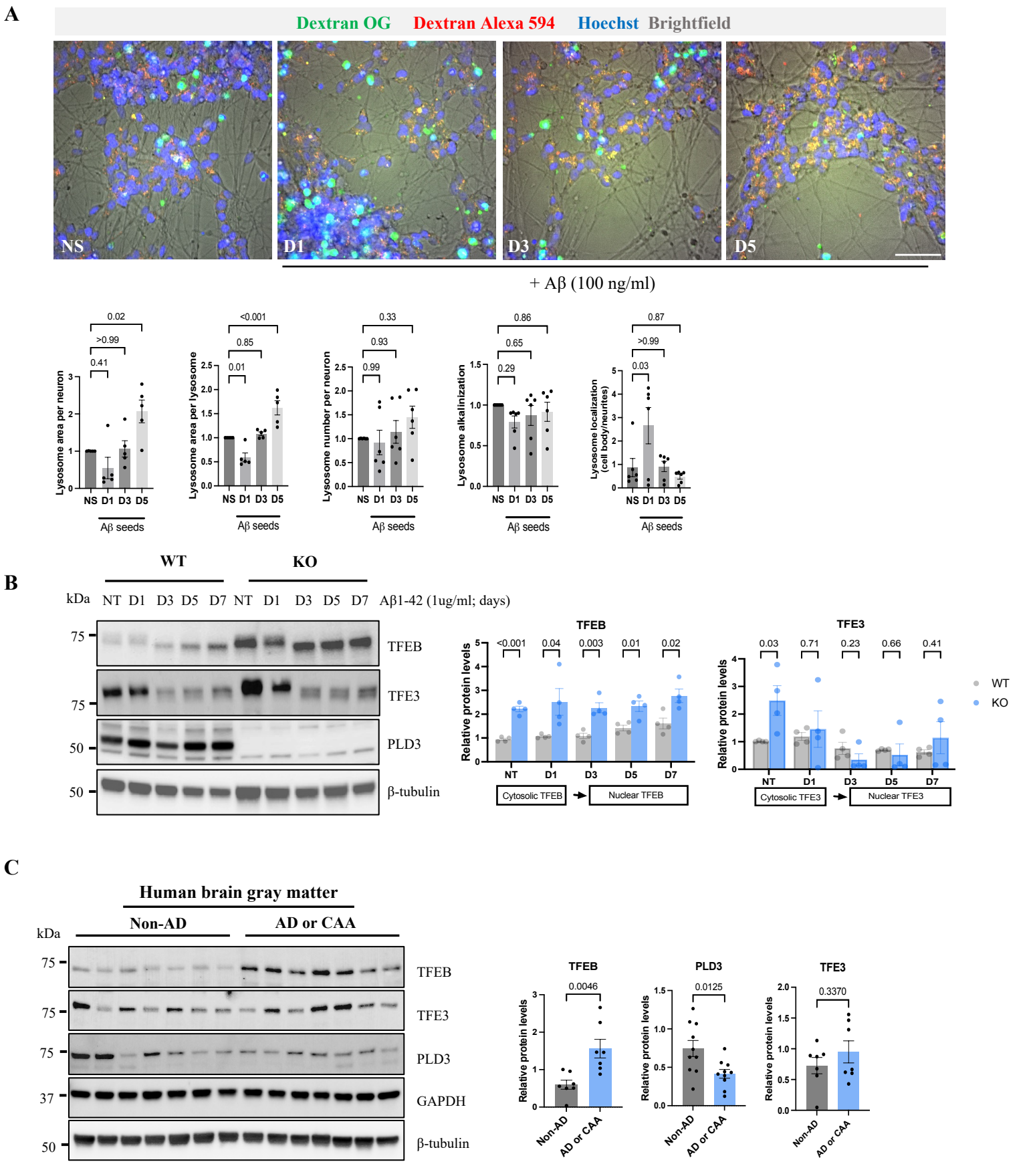

Fig 7. Loss of PLD3 potentially intensifies amyloid-induced lysosomal alterations and TFEB signaling.